

Calculating the tractive power and power conversion efficiency of battery electric vehicles using a global navigation satellite system and a road elevation database

Shinichi Domae¹, Alberto Castellazzi¹, Hamzeh J. Jaber¹, Tenghui Dong², Taketsune Nakamura²

¹KYOTO UNIVERSITY OF ADVANCED SCIENCE

18 Yamanouchi Gotanda-cho, Ukyo-ku,

Kyoto, 615-8577, Japan

+81-75-496-6254

domae.shinichi@kuas.ac.jp

²KYOTO UNIVERSITY

1-30, Goryo-Ohara, Nishikyo,

Kyoto, 615-8245, Japan

+81-75-383-3117

dong.tenghui.7v@kyoto-u.ac.jp

Acknowledgements

This research is supported by the discretionary budget of the President of Kyoto University of Advanced Technologies.

Keywords

«Data analysis», «Electric vehicle», «Efficiency»

Abstract

The energy conversion efficiency of battery electric vehicles (BEVs), which is an essential index in the development of motor systems, remains unknown during real driving. This paper presents a calculation method of the tractive power and energy conversion efficiency of BEVs during driving. The progress of the global navigation satellite system (GNSS) and the widespread use of road elevation database enable a tractive power measurement during driving. We have developed the calculation method to evaluate an advanced motor-drive for BEVs under development without using chassis dynamometers. The calculation method showed almost the same energy conversion efficiencies on the three different routes. The results demonstrate the universality of the method and raise the possibility of benchmarking of the power conversion efficiency of any of various BEVs.

Introduction

The energy conversion efficiency of battery electric vehicles (BEVs)—an essential index to expand the driving ranges of BEVs and to reduce the global energy consumption—remains unknown during driving. Chassis dynamometers, which have been used to evaluate the tractive powers of vehicles, cannot measure actual tractive powers during driving and involve higher costs. A tractive power and energy conversion efficiency calculation method with the longitudinal dynamic model has been developed to evaluate an advanced motor-drive for BEVs under development without using chassis dynamometers. The main input data for the calculation includes the locations, speeds, and altitudes of vehicles. The progress of the global navigation satellite system (GNSS) enables accurate measurement of location and speed, whereas the widespread use of road elevation databases allows access to precise altitude information. The method can calculate the tractive powers and energy conversion efficiencies during driving and requires lower costs. Many works have been reported regarding energy

consumption estimations for BEVs with the longitudinal dynamic model but their main purposes are precise predictions of driving ranges [1]. The paper presents a calculation method for BEV power train evaluations that can substitute the measurement with Chassis dynamometers. Almost same energy conversion efficiencies on the three different routes demonstrate sufficient universality achievable with the calculation method. The advanced motor system consisting of a 3-phase Y-inverter and a Halbach motor [2], which will be equipped to a small BEV, will be evaluated by the reported method in the near future.

Experiments

Tractive powers and energy conversion efficiencies are calculated with the longitudinal dynamic model which is well accepted and universal for any vehicles [3]. The major external forces acting on a vehicle include the following four forces: the rolling resistance of tires on road surfaces, F_{roll} , the aerodynamic drag during traveling at a particular speed in the air, F_{aero} , the grading resistance due to gravitation force, F_{grad} , and the acceleration resistance, F_{accel} . The traction force, F_{tract} , can be obtained as the sum of the four external force as follows. These forces are shown in Figure 1.

$$F_{tract} = F_{roll} + F_{aero} + F_{grad} + F_{accel} \quad (1)$$

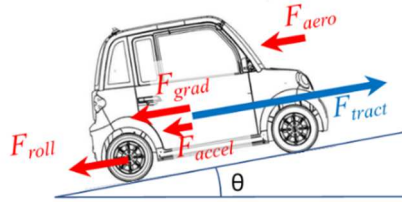


Fig. 1: Longitudinal dynamics of a vehicle

F_{roll} , F_{aero} , F_{grad} , and F_{accel} are expressed as follows,

$$F_{roll} = \mu mg \cos \theta \quad (2)$$

$$F_{aero} = \frac{1}{2} \rho C_d A (v + v_w)^2 \quad (3)$$

$$F_{grad} = mg \sin \theta \quad (4)$$

$$F_{accel} = (m + m_f) \frac{dv}{dt} \quad (5)$$

where μ is the rolling resistance coefficient, m is the vehicle mass, g is the gravitational acceleration, θ is the road inclination angle, ρ is the air density, C_d is the aerodynamic drag coefficient, A is the vehicle frontal area, v is the vehicle speed, v_w is the component of wind speed, m_f is the fictive mass of rolling inertia, and $\frac{dv}{dt}$ is the acceleration of the vehicle. The motor torque, T_m , and the motor speed, N_m (rpm), are calculated with the traction force and vehicle speed as shown below.

$$T_m = F_{tract} \frac{D_p}{2A_r} \quad (6)$$

$$N_m = 60A_r \frac{v}{\pi D_p} \quad (7)$$

where D_p is the diameter of the tire and A_r is the reduction ratio. The tractive power, P_{tract} , is calculated as a product of traction force and vehicle speed as below.

$$P_{tract} = F_{tract} v \quad (8)$$

The battery output power, P_{bat} , can be calculated with the battery output current and the battery output voltage obtained via a controller area network (CAN) bus. The power consumed by non-traction loads (auxiliary loads) are subtracted from P_{bat} . The brake booster, power steering, and wind wiper were the main auxiliary loads. The air conditioner or heater were not used during driving to avoid any unanticipated influences on the calculation. The energy conversion efficiency, η , can be calculated as

$$\eta = P_{tract} / P_{bat} \quad (9)$$

All the parameters for the model are shown in **Table I**. The locations and speeds of vehicles are measured by GNSS. The Quasi-Zenith Satellite System (QZSS) is available as GNSS in Japan since 2018. The sampling rate of the used GNSS system is 1 Hz. The road inclination angles, θ , are calculated by dividing the changes in elevation (m) per second by the horizontal vehicle velocities (m/sec) as shown in Fig. 2. The elevation information for each location measured by GNSS every second is obtained with using an open database of Geospatial Information Authority of Japan (GSI). The altitude of the driving route measured by GNSS and that obtained at the GSI database are compared in Figure 3. The altitude measured by GNSS (orange line) is instable because GNSS has larger error in vertical direction than in horizontal direction. The altitude obtained from the GSI database (blue line) is found to be much more stable. The use of the elevation database enables an accurate calculation of the road inclination angles. Air densities, ρ , are calculated by measuring the temperature, the relative humidity, and the atmospheric pressure during driving. Rolling resistance coefficient, μ , and aerodynamic drag coefficient, C_d , were obtained by coast down tests. Wind velocity, v_w , is assumed to be zero because it is relatively low and the measurement is practically difficult. Fictive mass of rolling inertia, m_f , is also assumed to be zero. The traction forces were calculated every second to synchronize with the sampling rate of the used GNSS system of 1 Hz.

Table I: Vehicle longitudinal dynamics equation parameters

Symbol	Meaning	Value (unit)
g	Gravitational Acceleration	9.81 (m/s ²)
θ	Road Angle	Variable (rad)
m	Vehicle Mass	616 + Passengers' Weight (kg)
v	Vehicle Speed	Variable (m/s)
μ	Rolling Resistance Coefficient	0.0122
ρ	Air Density	Variable (kg/m ³)
C_d	Aerodynamic Drag Coefficient	0.495
A	Vehicle Frontal Area	1.7 (m ²)
v_w	Wind Velocity	Assumed To Be Zero (m/s)
m_f	Fictive Mass of Rolling Inertia	Assumed To Be Zero (kg)
D_p	Tire Diameter	0.507 (m)
A_r	Reduction Ratio	6.07

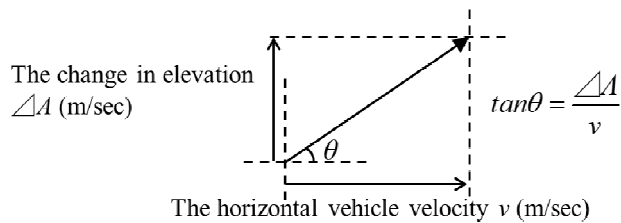


Fig. 2: The calculation of the road inclination angle θ

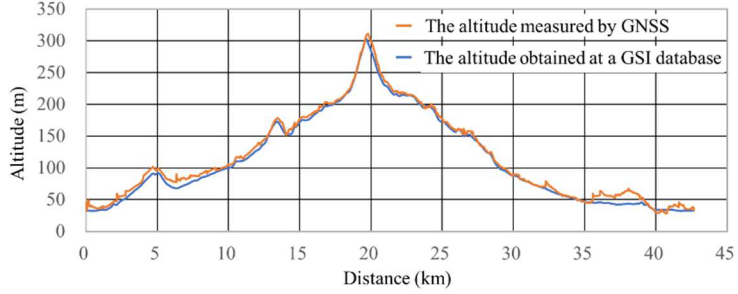


Fig. 3: The altitude of the driving route measured by GNSS and that obtained at a GSI database

The used test vehicle is a lightweight electric vehicle, TAJIMA-JIAYUAN. The vehicle, which has a simple structure and a simple control system, allows easy replacement of the Y-inverter and the Halbach motor under development with the present inverter and motor. The main characteristics of the test vehicle are shown in **Table II**. The maximum speed is 60 [km/h] and the regeneration energy is not available.

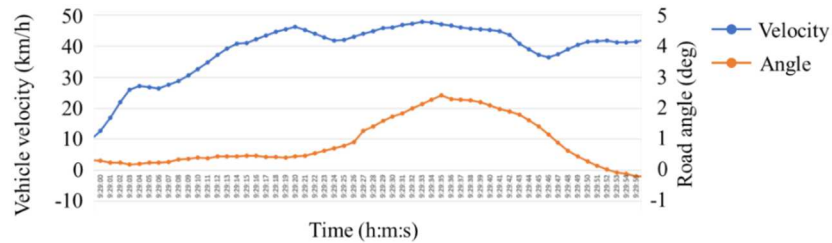
Table II: Test vehicle characteristics

Parameters	Value (unit)
Length/ Width/ Height	2,495 x 1,295 x 1,930 (mm)
Curb Weight	616 (kg)
Electric Motor Type	Induction Motor
Max. Power	16 (kW)
Max. Torque	101 (Nm)
Max. speed	60 (km/h)
Battery Capacity	10 (kWh)
Regeneration Energy	Not available

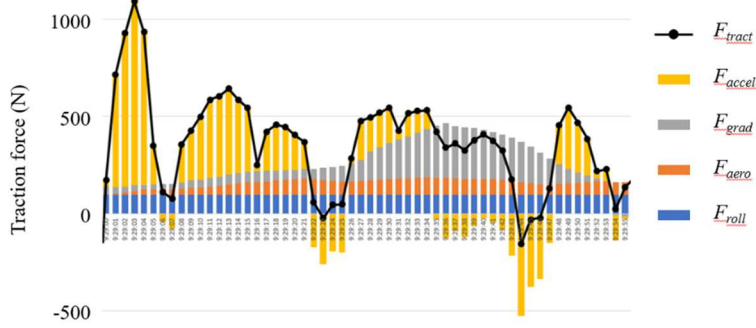
Results and Discussions

Torque-speed

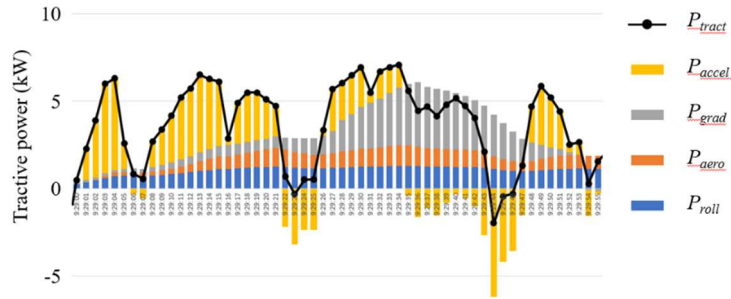
An example of the traction force, F_{tract} , and the tractive power, P_{tract} , are shown in Fig. 4. In Fig. 4 (a), the vehicle speed increases from 10 km/h to nearly 50 km/h and the road angle increases to about 2 degrees with time. In Fig. 4 (b), F_{tract} plotted on the black line graph and F_{roll} , F_{aero} , F_{grad} , and F_{accel} are plotted on the stacked column graphs of blue, orange, gray, and yellow, respectively. F_{roll} is almost constant. F_{aero} is proportional to the square of the velocity. F_{grad} increases with the road angle. F_{accel} changes corresponding to the acceleration and deceleration of the vehicle. In Fig. 4 (c), P_{tract} plotted on the black line graph and P_{roll} , P_{aero} , P_{grad} , and P_{accel} , which are work done per second against F_{roll} , F_{aero} , F_{grad} , and F_{accel} , are plotted on the stacked column graphs of blue, orange, gray, and yellow, respectively. As shown in this example, the calculation enables to visualize the changes of P_{tract} with the changes of the vehicle speed and road angle. Furthermore, it enables in-situ monitoring of P_{tract} if road elevation information is available during driving.



(a) Vehicle velocity ad Road angle



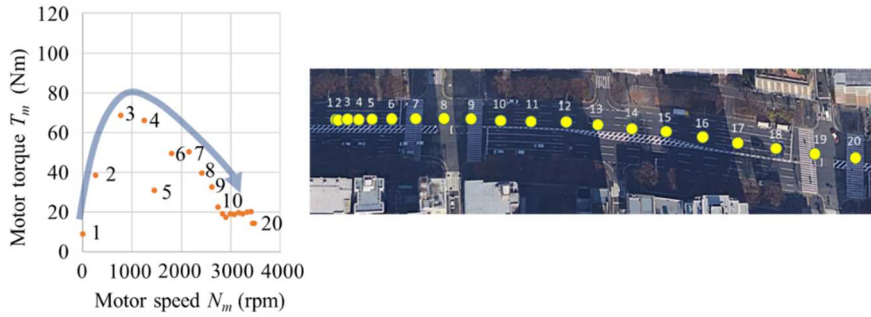
(b) The traction forces, F_{tract}



(c) The tractive powers, P_{tract}

Fig. 4: An example of the calculated traction forces F_{tract} and tractive powers P_{tract}

Fig. 5 (a) shows another example of the calculation: a scatter plot of the motor torque, T_m , and the motor speed, N_m , when the vehicle started at a green traffic signal. The numbers in the chart indicate the time by seconds after starting. The vehicle locations on the road are represented by yellow dots in Fig. 5 (b). N_m increases from 0 rpm to 3500 rpm which is equivalent to a car velocity from 0 km/h to 55 km/h. T_m increases to the maximum of 70 Nm to accelerate the vehicle and then decreases to 20 Nm which is required to keep speed constant against the rolling resistance and the aerodynamic drag. In general, the plot draws a trajectory shown as a blue arrow in Fig. 5 (a) and becomes almost constant.

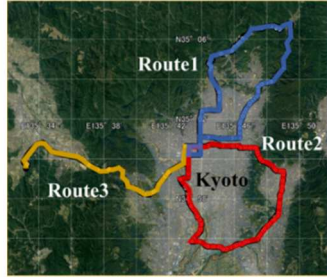


(a) Scatter plot of T_m and N_m

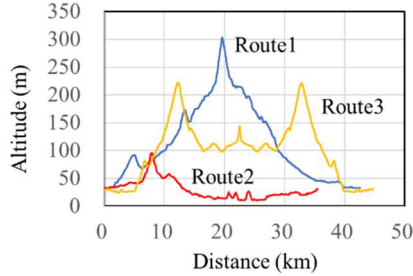
(b) Vehicle location

Fig. 5: Scatter plot of T_m and N_m when the vehicle started at a green traffic signal

Test runs were done on the three different routes in Kyoto (Route 1, Route 2, and Route 3) shown in Fig. 6 (a). Each route has different road gradients, and the Route 1 runs almost on a mountain road, the Route 2 runs in the city area and the Route 3 is in the middle as shown in the altitude profiles in Fig. 6 (b). The distances and numbers of test run of the routes are shown in **Table III**. Highways were not included in the routes because the test vehicle, which has the maximum speed of 60 km/h, is not allowed to run any highways.



(a) Map of the routes



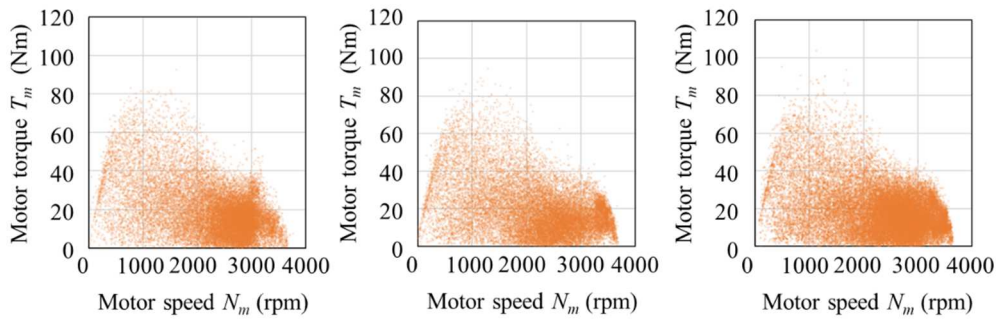
(b) Altitude profiles of the routes

Fig. 6: Maps and altitudes of the test courses

Table III: Information of routes

	ROUTE 1	ROUTE 2	ROUTE 3
Distance (km)	42.6	48.8	35.3
Number of Test Runs	12	12	12

Fig. 7 (a), (b), and (c) show scatter plots of T_m and N_m on Route 1, Route 2, and Route 3. Data for zero P_{bat} are removed from the plots because the vehicle is in coasting or friction braking when P_{bat} is zero. The regeneration braking is not available for the test vehicle. The scatter plots on the three routes show almost same tendency: T_m spread widely when N_m is smaller than around 2000 rpm and it becomes dense when N_m is larger than around 2000 rpm. Fig. 8 (a), (b), and (c) show the contour maps of the distribution of N_m and T_m on Route 1, Route 2, and Route 3, which are converted from the scatter plots shown in Fig. 7. The contour maps on the three routes have different shapes. Route 1 has the sharpest peak at around T_m of 18 Nm and N_m of 3000 rpm. This indicates that the vehicle was driven at almost constant torque and speed. Route 2 has a relatively broad peak and a tail spreading in the low speed and high torque region. Route 3 is in between. The difference of the shape among the routes should be due to traffic jams. In Route 1, the test vehicle runs at almost constant speed on mountain roads without traffic jams. In Route 2, the vehicle accelerates and decelerates repeatedly in the heavy traffic city area. As shown in Fig. 5 (a), higher torque is required in acceleration.

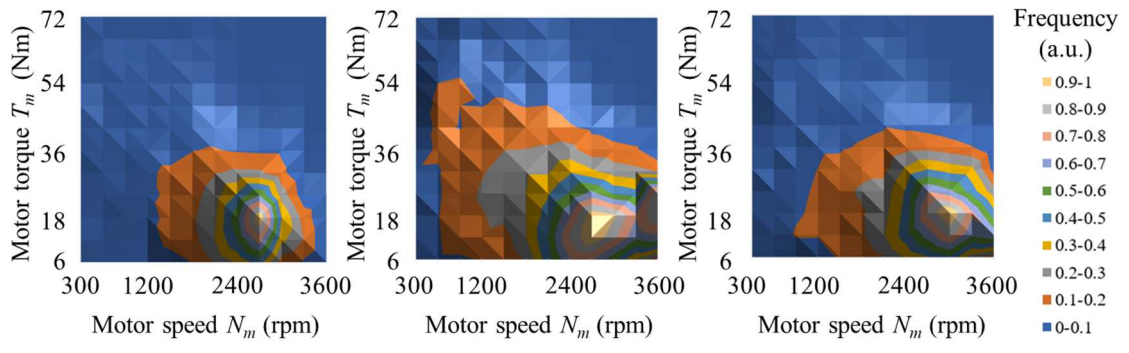


(a) Route 1

(b) Route 2

(c) Route 3

Fig. 7: The scatter plots of N_m and T_m for all runs on the three routes



(a) Route 1

(b) Route 2

(c) Route 3

Fig. 8: The contour maps of the distribution of N_m and T_m

Energy conversion efficiency

Fig. 9 (a), (b), and (c) show the energy conversion efficiency maps on the T_m - N_m planes measured on Route 1, Route 2, and Route 3. Fig. 9 use the same data sets as Fig. 7 and Fig. 8. The battery output powers, P_{bat} , are combined with the tractive powers, P_{tract} , to calculate the energy conversion efficiencies, η , for positive P_{bat} . The T_m - N_m plane is divided into small squares and the average energy conversion efficiency is calculated in each square after removing the outliers statistically. In Fig. 9, the three routes show almost the same efficiency maps even though the road slopes and the T_m - N_m distributions are different. Fig. 10 (a) and (b) show the close energy conversion efficiencies among routes at the motor torque T_m of 18 Nm and 30 Nm. The results demonstrate the sufficient universality to calculate the efficiency of the motor system achievable regardless of the routes. Furthermore, the results raise the possibility of benchmarking of power conversion efficiency of any of various BEVs on any vehicle locations on the globe using the road elevation information. The reported method will be used to evaluate the advanced motor system under development.

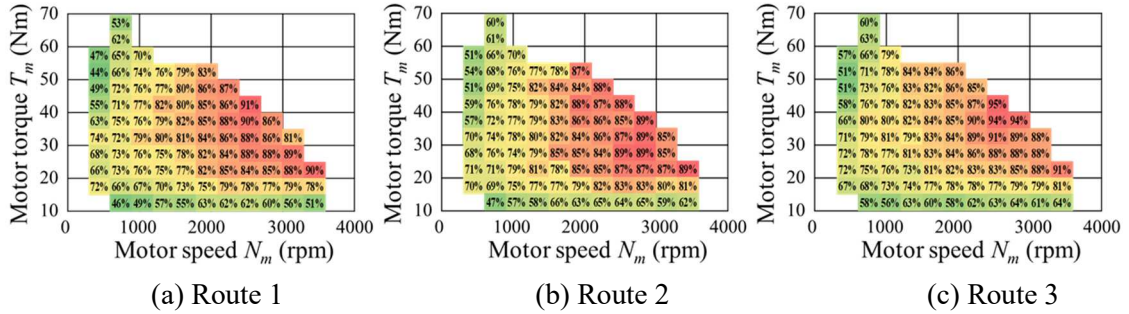


Fig. 9: The energy conversion efficiency maps for Route 1-3

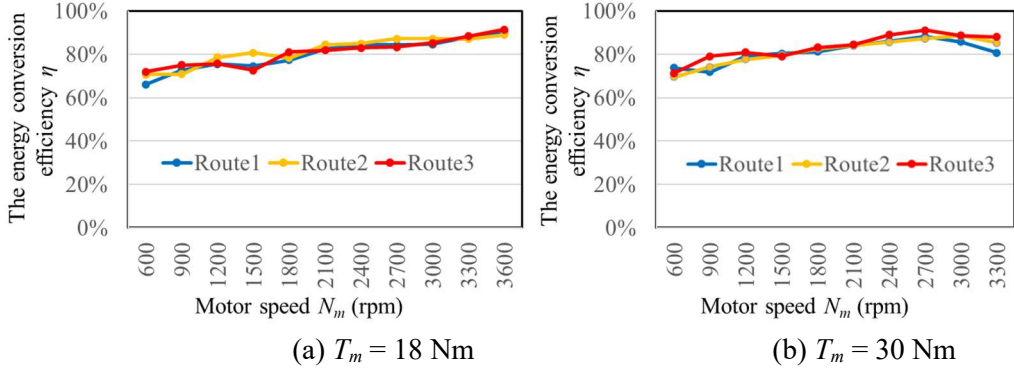


Fig. 10: The energy conversion efficiency for Route 1-3

Motor system

The advanced motor system consisting of a 3-phase Y-inverter and a Halbach motor is under development. An interleaved three-phase Y-inverter is introduced to the motor-drive [4]. The Y-inverter has some innovative features such as sinusoidal output voltage synthesis as opposed to square wave modulated, no high voltage DC-link, and integrated voltage boost capability. In addition, the discontinuous pulse width modulation (D-PWM) is adopted with the state-of-the-art wide-bandgap semiconductor power devices. The electrical design has been described in [2]. Fig. 11 shows the proposed three-phase Y-inverter's circuit diagram and a photograph of one-phase Y-inverter.

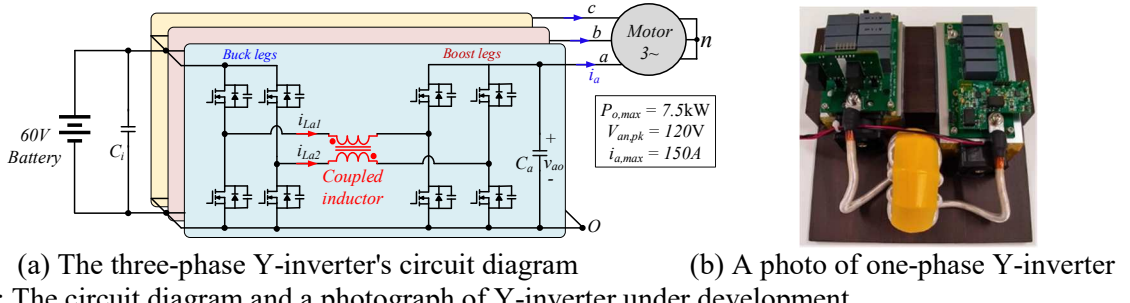
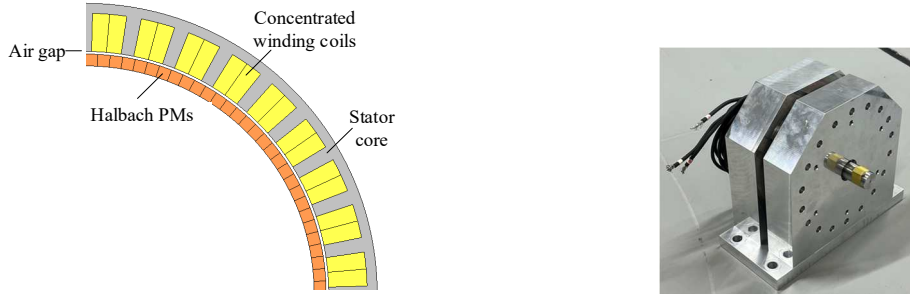


Fig. 11: The circuit diagram and a photograph of Y-inverter under development

The motor is a single-rotor Halbach motor, which is designed to operate at high voltage and high rotational speed with more than double power density as an equivalent traditional permanent magnet synchronous machine (PMSM) design. Fig. 12 shows the basic structure and a photograph of the single-rotor Halbach motor. It is designed to ensure very high efficiency at the most diverse and over as broad a range as possible of operational conditions, torque and speed. [2, 5, 6].



(a) The basic structure of the single-rotor Halbach motor (b) A photo of Halbach motor
Fig. 12: The basic structure and a photograph of the single-rotor Halbach motor

The required torques for the motor system under development were defined based on the T_m - N_m distribution discussed above. The inverter and motor design have been proceeded iteratively to optimize the joint performance and the power density for up to 5000 rpm and the full torque capability. The Y-inverter and the Halbach motor will replace the present inverter and motor of the test vehicle, and the energy conversion efficiency will be investigated by the reported calculation method in the near future.

Conclusions

A tractive force and energy conversion efficiency calculation method with the longitudinal dynamic model has been developed. The location and speed of a vehicle is obtained through GNSS and the elevation information is derived from an elevation database of GSI, which enables an accurate calculation of the road inclination angles. The visual information of dynamic behaviors and energy conversion efficiency of the vehicle can be obtained by the calculation method. The universality of the method is demonstrated by the almost same efficiencies on three different routes. The advanced motor system under development, which will be equipped to a small BEV, will be evaluated by the reported method in the near future. The calculation method discussed in this paper raises the possibility of benchmarking of the power conversion efficiency of any of various BEVs on any locations on the globe.

References

- [1] Chen, Y.: A Review and Outlook on Energy Consumption Estimation Models for Electric Vehicles, SAE J. STEEP 2(1):79-96, 2021
- [2] Tran H.: Low-voltage-battery powered hybrid-GaN/SiC Y-Inverter dual-rotor Halbach motor drive for light electric vehicles, in Proc. ICEMS 2021
- [3] Ehsani M.: Modern Electric, Hybrid Electric, and Fuel Cell Vehicles, CRC Press, 2005
- [4] Antivachis M.: Three-Phase Buck-Boost Y-Inverter with Wide DC Input Voltage Range, in Proc. APEC 2018
- [5] Kwak J.: Multi-parameter machine-inverter co-design for energy-efficient electric drives, in Proc. ICEMS2021
- [6] Dong T.: High Power-Density High-Efficiency Electric Drive Design with Halbach-Rotor PMSM and WBG-Based High-Frequency Inverter, in Proc. ICEMS2021